RSC Advances

PAPER

View Article Online
View Journal | View Issue

Cite this: *RSC Adv.*, 2017, **7**, 43636

Perchlorate ion doped polypyrrole coated ZnS sphere composites as a sodium-ion battery anode with superior rate capability enhanced by pseudocapacitance†

Tianyi Hou,[a] Guojie Tang,[a] Xiaohong Sun,[a]* Shu Cai,[a] Chunming Zheng*[b] and Wenbin Hu[a]

Received 18th July 2017
Accepted 5th September 2017

DOI: 10.1039/c7ra07901j

rsc.li/rsc-advances

Considering the inferior rate capability of conversion-type transition-metal sulphides (TMSs) caused by severe volume expansion and poor electronic conductivity, a composite of perchlorate ion (ClO_4^-) doped polypyrrole (PPy) coated ZnS spheres (denoted as ZnS@d-PPy) has been synthesized *via* a soft chemistry method. Benefiting from the improved conductivity, the protection of the PPy coating and ClO_4^- doping, ZnS@d-PPy exhibits decent cycling performance (419 mA h g^{-1} after 30 cycles at 100 mA g^{-1}) and superior rate capability (203 mA h g^{-1} at 4 A g^{-1}), which is enhanced by pseudocapacitance when being applied in sodium-ion batteries (SIBs).

1. Introduction

Sodium-ion batteries (SIBs) have drawn tremendous attention as a promising alternative to lithium-ion batteries (LIBs) because of the abundance and low cost of sodium resources.[1–4] The similar electrochemical reaction mechanism of Na^+ in SIBs to that of Li^+ in LIBs ensures the feasibility of SIBs.[1,5] Anode materials, an essential component of SIBs, often suffer from a low specific capacity[5,6] and one of the primary reasons is Na^+ (radius 1.06 Å, mass 23.0 g mol^{-1}) is larger and heavier than Li^+ (radius 0.76 Å, mass 6.9 g mol^{-1}).[7] For example, graphite cannot effectively intercalate sodium due to its small interlayer distance and a critical minimum spacing of 0.37 nm between graphitic layers has been demonstrated for carbon materials.[8,9] Some researchers made efforts on hard carbon materials because of their large interlayer distance; however, most of them delivered a reversible capacity below 300 mA h g^{-1}.[8] Although exhibiting good cyclability, other intercalation-type anode materials such as expanded graphite,[9] $Na_2Ti_3O_7$ (ref. 10 and 11) and $NaTi_2(PO_4)_3$ (ref. 12) also have the same problem of a low capacity. By contrast, alloying and conversion anode materials with relatively high theoretical capacity are proposed to address this problem. Although silicon, an important alloying anode material for LIBs, does not alloy with sodium at room temperature, tin is a promising alloying anode material for SIBs with an average voltage of 0.3 V and a theoretical capacity of 790 mA h g^{-1}.[4] Conversion anode materials such as Fe_2O_3 (ref. 5) and Co_3O_4 (ref. 13) have been also extended to SIBs due to their multiple electron reactions accompanied with high theoretical specific capacities.[1] Recently, transition-metal sulphides (TMSs) anode materials with conversion reaction mechanisms have been paid much attention for their higher theoretical capacities,[6] unique physical and chemical properties.[14] Among various TMSs, ZnS is a competitive candidate for SIB anode materials because of its high theoretical capacity (550 mA h g^{-1}), low cost, non-toxic nature[14–16] and has been carefully investigated in LIBs.[17–22] However, it is always limited by a quick capacity fading and poor rate capability caused by low electronic conductivity and severe volume change during discharge/charge processes.[15,22] Synthesizing hollow structure is a good approach to alleviate the volume-expansion issue and hollow interiors can effectively accommodate volume variation during discharge/charge processes.[23,24] N. Du *et al.* synthesized ZnS hollow spheres used SiO_2 spheres as templates and a layer-by-layer approach for applying in LIBs.[25] However, hollow structure anode materials are still hindered by a low volumetric energy density and side reactions due to their large void space and high surface areas.[23]

Another general approach is to fabricate composites of ZnS and carbonaceous materials such as graphene,[14,22] porous carbon[21] and nitrogen-doped carbon.[15] W. Qin *et al.* elevated the specific capacity of active materials by embedded ZnS nanoparticles in reduced graphene oxide, delivering a reversible capacity of 610 mA h g^{-1} at 100 mA g^{-1}.[14] J. Li *et al.* have

[a]*School of Materials Science and Engineering, Key Laboratory of Advanced Ceramics and Machining Technology of Ministry of Education, Tianjin University, Tianjin 300072, PR China. E-mail: sunxh@tju.edu.cn*

[b]*State Key Laboratory of Hollow-fiber Membrane Materials and Membrane Processes, School of Environmental and Chemical Engineering, Tianjin Polytechnic University, Tianjin 300387, PR China. E-mail: zhengchunming@tjpu.edu.cn*

† Electronic supplementary information (ESI) available. See DOI: 10.1039/c7ra07901j

reported urchinlike ZnS microspheres decorated with N-doped carbon derived from polydopamine and they exhibited superior electrochemical performance as an anode material for both LIBs and SIBs.[15] These results demonstrate that conductive coating is a valid method of improving the behavior of ZnS-based anode materials. Polypyrrole (PPy) as a well-known conductive polymer has been extensively applied in the battery field (*e.g.*, lithium sulfur batteries,[26] LIBs[27–29] and SIBs[30–32]) with simple synthesis and possibly works on ZnS-based anodes. Meanwhile, PPy layers are also highly stretchable and flexible, allowing free volume variation and accommodating volume expansion of anodes during sodiation/desodiation processes.[32] However, too much PPy coating will lead to a lower actual capacity. Perchlorate ions (ClO_4^-) doping is an effective method to increase the conductivity[33] and acts as redox-active sites to improve the capacity of PPy coated active materials reported by W. Li *et al.* on Prussian blue analog (PBA) cathodes of SIBs.[31] it is also meaningful to investigate the behavior of d-PPy coating in anode materials.

Herein, we report a composite of thin-layer (~15 nm) ClO_4^- doped PPy (d-PPy) coated ZnS spheres (denoted as ZnS@d-PPy) *via* a soft chemistry method. The as-prepared ZnS@d-PPy exhibits superior rate capability. Further kinetic analyses reveal that the behavior of ZnS@d-PPy is enhanced by pseudocapacitance as well as the effectiveness of d-PPy coating improving the conductivity of the composite and maintaining the structural integrity.

2. Experimental

2.1. Material synthesis

The synthesis consists of two steps: the preparation of ZnS spheres and d-PPy coating process. The preparation of ZnS followed the previous work[34] with the concentration of thiourea was 1 M. The d-PPy coating process was modified from the previous research.[26,31] 100 mg above prepared ZnS spheres were dispersed in 40 ml dimethyl carbonate (DMC) by ultrasound and then 24 mg $NaClO_4$ and 20 ml DMC solution of pyrrole (2.25 mM) was added. Next, 10 ml DMC solution of $FeCl_3$ (0.25 mM) was slowly added as an oxidant under vigorous stirring in ice bath for 1 h. Finally, ZnS@d-PPy was collected by centrifugation and washed by ethanol for several times. Then as-prepared powder was dried at 60 °C in a vacuum oven overnight. For comparison, the composite of ZnS spheres coated by pure PPy (ZnS@PPy) was synthesized by the similar method without adding of $NaClO_4$.

2.2. Characterization

ZnS@d-PPy was characterized by X-ray diffraction (XRD, Bruker D8, Cu Ka radiation), Fourier transform infrared spectroscopy (FTIR, BIO-RAD FTS3000), Thermogravimetric analysis (TGA, STA449C), Field-emission scanning electron microscopy (SEM, JEOL JEM-2100F) and Transmission electron microscopy (TEM, JEOL JEM-2100F).

2.3. Electrochemical measurements

The electrodes were prepared by pasting slurries composed of 70% active materials, 20% carbon black and 10% poly (vinylidene fluoride) (PVDF) in the *N*-methyl-2-pyrrolidone (NMP) on copper foils and cutting into 10 mm disks with an active material loading rate of around 0.8 mg cm^{-2}. CR2032 coin-type cells were assembled with sodium foils as both reference and counter electrodes and glass fiber membranes (Whatman) as separators. The electrolyte was 1 M sodium trifluomethanesulfonate ($NaSO_3CF_3$) in diglyme (DGM). Galvanostatic tests were cycled between 0.01–3 V at room temperature by using the LAND CT2001A battery-testing instrument. The specific capacity was calculated based on the total mass of active materials. Cyclic voltammograms (CVs) were performed between 0–3 V on an electrochemical workstation (CHI660C, Chenhua, Shanghai, China). Electrochemical impedance spectroscopy (EIS) measurements were conducted by employing an AC voltage of 5 mV amplitude with a frequency range from 100 kHz to 0.01 Hz.

3. Results and discussion

Fig. 1a shows the X-ray diffraction (XRD) patterns of ZnS and ZnS@d-PPy. All the main peaks in the XRD patterns can be indexed to the standard JCPDS no. 05-0492, indicating a hexagonal ZnS with the $P6_3mc$ space group (wurtzite structures).[34] The similarity of XRD patterns between ZnS and ZnS@d-PPy suggests that the polymerization of pyrrole with $FeCl_3$ oxidant and $NaClO_4$ dopant cause no damage to crystalline structure of ZnS and no detectable impurity is introduced. In Fig. 1b the intensity of the spectrum of ZnS@d-PPy is slightly lower than that of ZnS and the obvious bands at ~1560 and ~936 cm^{-1} of ZnS@d-PPy can be assigned to C–C stretching vibration in pyrrole ring and perchlorate ions, respectively, indicating the outermost coating of the d-PPy layer.[29,31,33] The mass ratio of d-PPy is 8.9% for ZnS@d-PPy from the TGA curves (ESI, Fig. S1†), which indicates a low d-PPy content of the ZnS@d-PPy composite.

Fig. 2 shows the SEM and TEM images of ZnS and ZnS@d-PPy. From Fig. 2a, it can be seen that ZnS spheres have a homogeneous size distribution of about 300 nm. And ZnS nanograins (10–40 nm) can be found on the surface of ZnS spheres after zooming in (Fig. 2b). After d-PPy coating, the spherical diameter of ZnS@d-PPy spheres is still uniform and similar to ZnS spheres (Fig. 2d). The surface of ZnS@d-PPy

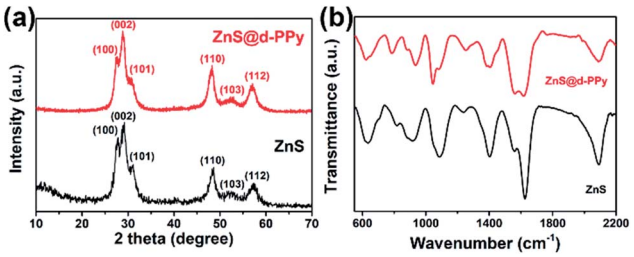

Fig. 1 (a) XRD patterns and (b) FTIR spectra of ZnS and ZnS@d-PPy.

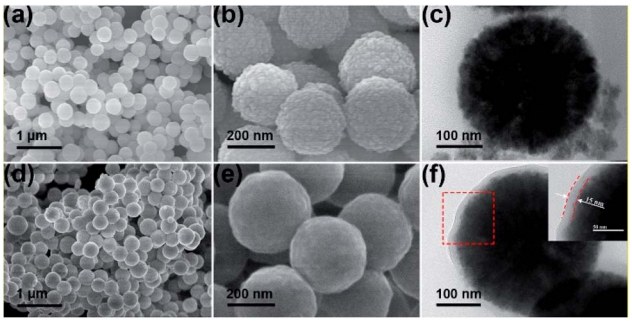

Fig. 2 (a, b) SEM and (c) TEM images of ZnS; (d, e) SEM and (f) TEM images of ZnS@d-PPy. Inset of (f) is the high-magnification image of the selected area in the red dash line.

spheres become smooth, indicating the cover of d-PPy layers (Fig. 2e). ZnS@PPy without adding of $NaClO_4$ has an identical morphology with ZnS@d-PPy (ESI, Fig. S2†), suggesting ClO_4^- has less impact on d-PPy coating processes. More details can be found in TEM images of ZnS (Fig. 2c) and ZnS@d-PPy (Fig. 2f), where ZnS nanograins are uniformly distributed in a spherical particle with a mesoporous property (ESI, Fig. S3†). Fig. 2f depicts that ZnS is coated by a thin d-PPy layer with an average thickness of about 15 nm. By comparison, d-PPy coating bring no significant change to the morphology of ZnS spheres.

The electrochemical performance of ZnS and ZnS@d-PPy composite electrodes were investigated by using CR2032 coin-type Na half cells. Fig. 3a and b show the CV curves of ZnS and ZnS@d-PPy *versus* Na^+/Na between 0 and 3 V at a scan rate of 0.1 mV s^{-1}. For ZnS, in the first cathodic scan, a weak peak at around 0.60 V corresponds to Na^+ insertion into ZnS and the following strong peaks at 0.35 V and 0.10 V are assigned to the conversion reaction of ZnS and the formation of solid electrolyte interface (SEI) layers.[14–16] The situation is similar for ZnS@d-PPy while only one merged strong peak appears at around 0.34 V. In second and third cathodic scans, three peaks can still be found at about 0.62, 0.45 and 0.03 V for both ZnS and ZnS@d-PPy. As for anodic scans, peaks between 0.50 and 1.30 V can be attributed to several steps of extraction of Na^+ from Na_2S and the formation of ZnS. A broad peak at around 1.50 V only appears in CV curves of ZnS@d-PPy is most likely due to ClO_4^- doping providing redox-active sites.[31] The possible sodiation/desodiation mechanism of ZnS is described below:

$$2Na^+ + ZnS + 2e^- \leftrightarrow Na_2S + Zn \quad (1)$$

Fig. 3c and d show the discharge/charge profiles of ZnS and ZnS@d-PPy. For pure ZnS, the initial discharge curve presents two plateaus below 0.5 V while there is one major plateau for that of ZnS@d-PPy and it is similar to the first cathodic scan in CV curves of ZnS and ZnS@d-PPy, corresponding to the conversion reaction of ZnS. In following discharge processes, the platform voltage elevates to around 0.7 V for both ZnS and ZnS@d-PPy in discharge/charge profiles and the similar condition also occurs in CV curves, mainly owing to the irreversible formation of SEI layers and irreversible changes of ZnS after the initial sodiation/desodiation process, which still needs further investigation. In Fig. 3c, pure ZnS delivers a discharge and charge capacity of 880 and 563 mA h g^{-1} in the first cycle at 100 mA g^{-1} with a coulombic efficiency of 63.9%. After d-PPy coating, the initial discharge and charge capacity of ZnS@d-PPy is 775 and 507 mA h g^{-1}. And the coulombic efficiency is 65.4%, which is slightly higher than pure ZnS. The capacity loss of the first cycle is mostly out of the formation of SEI layers.[14,15] The main reason for the higher initial capacity of ZnS than that of ZnS@d-PPy is because that the specific capacity of ZnS@d-PPy is calculated on the basis of the total mass of ZnS@d-PPy and d-PPy has a lower specific capacity than ZnS.[31]

Fig. 4a shows the cycling performance of ZnS, ZnS@PPy and ZnS@d-PPy between 0.01 and 3 V at 100 mA g^{-1}. As we can see,

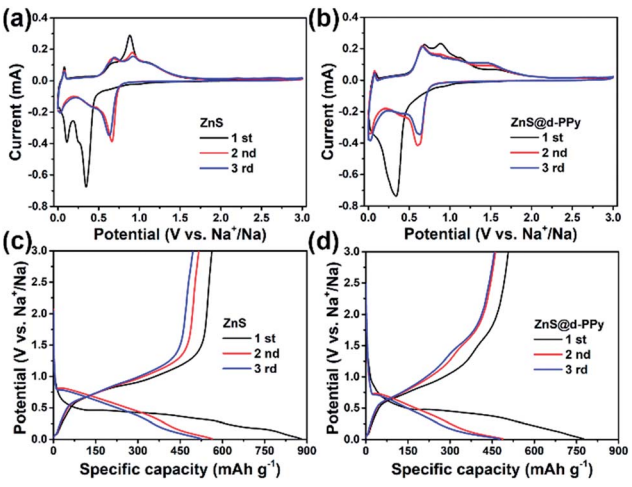

Fig. 3 CV curves of (a) ZnS, (b) ZnS@d-PPy between 0 and 3 V at a scan rate of 0.1 mV s^{-1}; discharge/charge voltage profiles of (c) ZnS, (d) ZnS@d-PPy between 0.01 and 3 V at 100 mA g^{-1} for the initial three cycles.

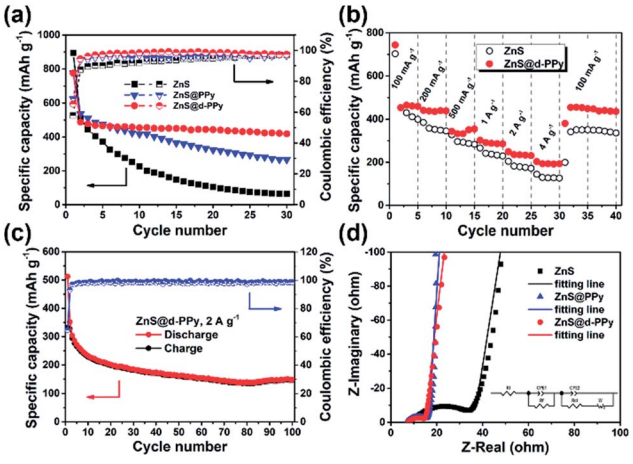

Fig. 4 (a) Cycling performance of ZnS, ZnS@PPy and ZnS@d-PPy at 100 mA g^{-1}; (b) rate capability of ZnS and ZnS@d-PPy; (c) long-term cycling stability of ZnS@d-PPy at 2 A g^{-1}; (d) partial Nyquist plots of ZnS, ZnS@PPy and ZnS@d-PPy after initial cycle. The equivalent circuit is shown as inset.

ZnS@d-PPy has the best cycling performance among three samples, delivering 419 mA h g^{-1} after 30 cycles (ESI, Fig. S4†). ZnS@PPy and ZnS@d-PPy show better cycling stability than pure ZnS (64 mA h g^{-1} after 30 cycles), indicating PPy coating has a positive effect as a conductive and buffer layer accommodating the volume expansion and protecting ZnS spheres form being destroyed during discharge/charge processes. Compared with ZnS@PPy (266 mA h g^{-1} after 30 cycles), ZnS@d-PPy retains a higher discharge capacity over 30 cycles, demonstrating ClO_4^- doping is effective and provides more capacity to the composite than pure PPy coating. Fig. 4b displays the rate capability of ZnS and ZnS@d-PPy. ZnS@d-PPy exhibits superior rate capability and delivers discharge capacities of 465, 441, 355, 302, 249 and 203 mA h g^{-1} at 100, 200, 500, 1000, 2000 and 4000 mA g^{-1}, respectively. And after the current returns to 100 mA g^{-1}, a capacity retention of about 98% is achieved (455 mA h g^{-1}) while that of ZnS is ~77%. Discharge/charge voltage profiles of each current can also be seen in Fig. S5 ESI.† Meanwhile, the long-term cycling performance of ZnS@d-PPy was investigated at a high current density of 2 A g^{-1} (Fig. 4c). After 100 cycles, a discharge capacity of 148 mA h g^{-1} with a high coulombic efficiency (98.5%) can be still retained. More evidence can be found in Nyquist plots (Fig. 4d), where ZnS@d-PPy exhibits lowest charge-transfer resistance (5.6 Ω) than that of ZnS (19.7 Ω) and ZnS@PPy (6.4 Ω) after initial cycle at 100 mA g^{-1}. It suggests that d-PPy coating can effectively enhance the conductivity of the ZnS@d-PPy composite.

Considering superior rate capability of ZnS@d-PPy, it can be theorized that electrochemical capacitance effects have an important impact on fast discharge/charge processes.[35,36] Herein, a quantitative analysis based on CV tests at various scan rates was used for further investigating the reaction kinetic of ZnS@d-PPy and distinguishing between capacitive and diffusion-controlled contributions to the total capacity. The CV curves at scan rates of 0.1, 0.3, 0.6, 0.9 and 1.2 mV s^{-1} are shown in Fig. 5a. The shapes of each curve are identical with peak currents gradually increasing as scan rates ascending. The measured current (i) obeys a power law relationship with the scan rate (v) according to

$$i = av^b. \quad (2)$$

Both a and b are adjustable parameters. In particular, $b = 0.5$ represents a diffusion-controlled faradaic intercalation process, while $b = 1$ indicates a capacitive behavior *via* a surface faradaic redox reaction.[6,37] The slope of log(i) *vs.* log(v) plots are the b-values and the calculated b-values are 0.57, 0.75, 0.92 and 1.00 for R1, R2, O1 and O2 peaks, respectively (Fig. 5b).

To distinguish quantitatively the capacitive contribution from the current response, eqn (2) is rewritten as

$$i(V) = k_1v + k_2v^{1/2}. \quad (3)$$

In eqn (3), k_1v and $k_2v^{1/2}$ can attribute to capacitive and diffusion-controlled contributions.[35,37] For analytical purposes, eqn (3) is rearranged as follows:

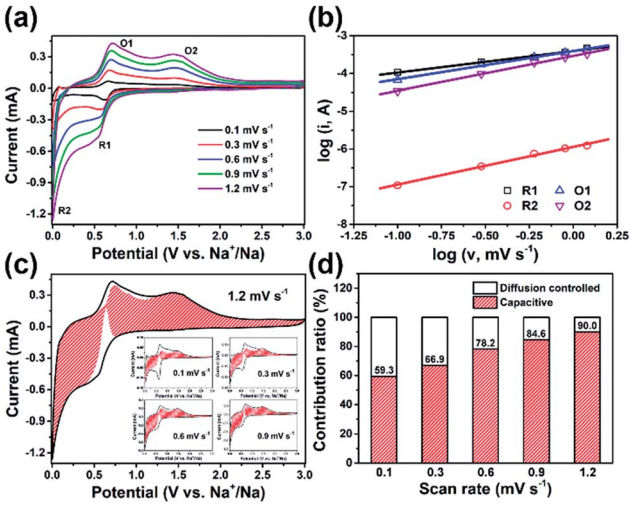

Fig. 5 (a) CV curves at various scan rates. (b) Determination of corresponding b-values of different redox states; (c) CV curves with separation of capacitive currents (red shaded region) among total currents (solid line) and (d) contribution ratios of the capacitive and diffusion-controlled capacity at various scan rates.

$$i(V)/v^{1/2} = k_1v^{1/2} + k_2 \quad (4)$$

By plotting $v^{1/2}$ *vs.* $i/v^{1/2}$, k_1 and k_2 can be derived from values of the slopes and intercepts. As in Fig. 5c, CV curves and capacitive contributions (shaded area) of each scan rate are shown. And as the scan rate increases from 0.1 to 1.2 mV s^{-1}, the proportion of surface capacitive capacity upgrades from 59.3 to 90.0% (Fig. 5d). The high contribution of the capacitive charge storage of ZnS@d-PPy may be accounted for that d-PPy coating enhances the conductivity of the composite and provides more redox-active sites[31] as well as ZnS nanograins shorten the Na^+ diffusion length.[6,16] The capacitive contribution is mainly provided by faradic charge-transfer process through surface atoms, referred to as pseudocapacitance, generally.[16,37] As a result, the dominated pseudocapacitive Na^+ storage mechanism enhances the high-rate capability of ZnS@d-PPy.

Fig. 6 shows the structure evolution of ZnS and ZnS@d-PPy investigated by ex situ SEM and TEM images. Combined with the schematic illustration of ZnS (Fig. 6a) and corresponding SEM (Fig. 6b) and TEM (Fig. 6c) images, it is clear that the

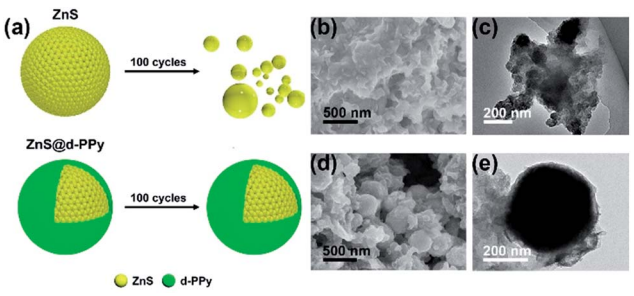

Fig. 6 (a) Schematic illustrations of structure evolution of ZnS and ZnS@d-PPy after 100 cycles at 2 A g^{-1} and corresponding (b), (d) SEM and (c), (e) TEM images, respectively.

structure of ZnS spheres collapse and significantly aggregate after cycles. That is because the sodiation of ZnS spheres causes drastic volume expansion and leads to the decomposition of ZnS spheres and deterioration of pure ZnS electrodes. In comparison, ZnS@d-PPy spheres still maintain their original core–shell structure without obvious changes (Fig. 6d and e) benefitting from the stretchable d-PPy coating accommodating volume expansion and stabilizing the structure of ZnS@d-PPy upon long-term cycling. All these demonstrate d-PPy coating can efficiently protect ZnS spheres from being wrecked and accommodate large volume expansion during sodiation even at a large current of 2 A g^{-1}.

The superior rate capability and good cyclability of ZnS@d-PPy can be attributed to two features by reviewing above results and analyses. First, the stretchable d-PPy coating increases the electronic conductivity of ZnS and act as a buffer layer to accommodate the volume expansion and maintain the structural integrity during discharge/charge processes. Second, d-PPy can provide more redox-active sites increasing the specific capacity and enhancing the electrochemical performance of ZnS@d-PPy composites, especially for the rate capability. Thereinto, ClO_4^- doping plays a crucial role for further improving the electronic conductivity of PPy and provides redox-active sites for sodium storage. Consequently, ZnS@d-PPy presents enhanced and efficient pseudocapacitive behavior and delivers a high-rate performance compared to the previous work of ZnS-based anodes in SIBs (Table S1†). In addition, the usage of ether-based $NaSO_3CF_3$/diglyme electrolyte is also beneficial to ZnS anodes according to previous work.[16,38]

4. Conclusions

In summary, a composite of ClO_4^- doped PPy coated ZnS spheres (~300 nm) has been successfully synthesized *via* a soft chemistry method with a d-PPy layer thickness of about 15 nm. When being applied as an anode material for SIBs, ZnS@d-PPy achieves a high specific capacity of 419 mA h g^{-1} at 100 mA g^{-1} after 30 cycles. More importantly, ZnS@d-PPy exhibits a superior rate capability and delivers a discharge capacity of 203 mA h g^{-1} at 4 A g^{-1}, and a capacity retention of about 98% is achieved after the current returns to 100 mA g^{-1}. This work provides a general approach for elevating electrochemical performance of anode materials with severe volume variation upon cycling and ClO_4^- doping also has potential to extend to the syntheses of other anode materials.

Conflicts of interest

There are no conflicts to declare.

Acknowledgements

The authors acknowledge the financial support by the National Natural Science Foundation of China, NSFC (51572192, 51472179, 51772205, 51772208) and General Program of Municipal Natural Science Foundation of Tianjin (17JCYBJC17000, 17JCYBJC22700).

Notes and references

1 S. W. Kim, D. H. Seo, X. H. Ma, G. Ceder and K. Kang, *Adv. Energy Mater.*, 2012, **2**, 710–721.
2 H. L. Pan, Y. S. Hu and L. Q. Chen, *Energy Environ. Sci.*, 2013, **6**, 2338–2360.
3 N. Yabuuchi, K. Kubota, M. Dahbi and S. Komaba, *Chem. Rev.*, 2014, **114**, 11636–11682.
4 D. Kundu, E. Talaie, V. Duffort and L. F. Nazar, *Angew. Chem., Int. Ed.*, 2015, **54**, 3431–3448.
5 N. Zhang, X. P. Han, Y. C. Liu, X. F. Hu, Q. Zhao and J. Chen, *Adv. Energy Mater.*, 2015, **5**, 1401123.
6 L. Zhou, K. Zhang, J. Sheng, Q. An, Z. Tao, Y.-M. Kang, J. Chen and L. Mai, *Nano Energy*, 2017, **35**, 281–289.
7 M. D. Slater, D. Kim, E. Lee and C. S. Johnson, *Adv. Funct. Mater.*, 2013, **23**, 947–958.
8 Y. L. Cao, L. F. Xiao, M. L. Sushko, W. Wang, B. Schwenzer, J. Xiao, Z. M. Nie, L. V. Saraf, Z. G. Yang and J. Liu, *Nano Lett.*, 2012, **12**, 3783–3787.
9 Y. Wen, K. He, Y. J. Zhu, F. D. Han, Y. H. Xu, I. Matsuda, Y. Ishii, J. Cumings and C. S. Wang, *Nat. Commun.*, 2014, **5**, 4033.
10 H. L. Pan, X. Lu, X. Q. Yu, Y. S. Hu, H. Li, X. Q. Yang and L. Q. Chen, *Adv. Energy Mater.*, 2013, **3**, 1186–1194.
11 A. Rudola, K. Saravanan, C. W. Mason and P. Balaya, *J. Mater. Chem. A*, 2013, **1**, 2653–2662.
12 Q. Zhang, C. Y. Liao, T. Y. Zhai and H. Q. Li, *Electrochim. Acta*, 2016, **196**, 470–478.
13 Y. P. Zhou, W. P. Sun, X. H. Rui, Y. Zhou, W. J. Ng, Q. Y. Yan and E. Fong, *Nano Energy*, 2016, **21**, 71–79.
14 W. Qin, D. Li, X. Zhang, D. Yan, B. Hu and L. Pan, *Electrochim. Acta*, 2016, **191**, 435–443.
15 J. Li, Y. Fu, X. Shi, Z. Xu and Z. Zhang, *Chem.–Eur. J.*, 2017, **23**, 157–166.
16 D. Su, K. Kretschmer and G. Wang, *Adv. Energy Mater.*, 2016, **6**, 1501785.
17 J. Wang, G. Wang, L. Yang, S. H. Ng and H. Liu, *J. Solid State Electrochem.*, 2006, **10**, 250–254.
18 N. Du, H. Zhang, J. Chen, J. Sun, B. Chen and D. Yang, *J. Phys. Chem.*, 2008, **112**, 14836–14842.
19 L. He, X.-Z. Liao, K. Yang, Y.-S. He, W. Wen and Z.-F. Ma, *Electrochim. Acta*, 2011, **56**, 1213–1218.
20 G. D. Park, S. H. Choi, J.-K. Lee and Y. C. Kang, *Chem.–Eur. J.*, 2014, **20**, 12183–12189.
21 Y. Fu, Z. Zhang, X. Yang, Y. Gan and W. Chen, *RSC Adv.*, 2015, **5**, 86941–86944.
22 M. Mao, L. Jiang, L. Wu, M. Zhang and T. Wang, *J. Mater. Chem. A*, 2015, **3**, 13384–13389.
23 L. Yu, H. Hu, H. B. Wu and X. W. Lou, *Adv. Mater.*, 2017, **29**, 39.
24 M. Wang, Y. Huang, X. Chen, K. Wang, H. Wu, N. Zhang and H. Fu, *J. Alloys Compd.*, 2017, **691**, 407–415.
25 N. Du, H. Zhang, J. Chen, J. Y. Sun, B. D. Chen and D. R. Yang, *J. Phys. Chem. B*, 2008, **112**, 14836–14842.

26 W. Li, Q. Zhang, G. Zheng, Z. W. Seh, H. Yao and Y. Cui, *Nano Lett.*, 2013, **13**, 5534–5540.
27 F. Han, D. Li, W.-C. Li, C. Lei, Q. Sun and A.-H. Lu, *Adv. Funct. Mater.*, 2013, **23**, 1692–1700.
28 D. Lepage, C. Michot, G. Liang, M. Gauthier and S. B. Schougaard, *Angew. Chem., Int. Ed.*, 2011, **50**, 6884–6887.
29 J. Yuan, C. Chen, Y. Hao, X. Zhang, B. Zou, R. Agrawal, C. Wang, H. Yu, X. Zhu, Y. Yu, Z. Xiong, Y. Luo, H. Li and Y. Xie, *J. Alloys Compd.*, 2017, **691**, 34–39.
30 M. Zhou, L. Zhu, Y. Cao, R. Zhao, J. Qian, X. Ai and H. Yang, *RSC Adv.*, 2012, **2**, 5495–5498.
31 W.-J. Li, S.-L. Chou, J.-Z. Wang, J.-L. Wang, Q.-F. Gu, H.-K. Liu and S.-X. Dou, *Nano Energy*, 2015, **13**, 200–207.
32 H. Liang, J. Ni and L. Li, *Nano Energy*, 2017, **33**, 213–220.
33 C. Tohumcu, R. Tas and M. Can, *Ionics*, 2014, **20**, 1687–1692.
34 H. J. Liu, Y. H. Ni, M. Han, Q. Liu, Z. Xu, J. N. Hong and X. Ma, *Nanotechnology*, 2005, **16**, 2908–2912.
35 S. Lou, X. Cheng, Y. Zhao, A. Lushington, J. Gao, Q. Li, P. Zuo, B. Wang, Y. Gao, Y. Ma, C. Du, G. Yin and X. Sun, *Nano Energy*, 2017, **34**, 15–25.
36 C. Chen, Y. Wen, X. Hu, X. Ji, M. Yan, L. Mai, P. Hu, B. Shan and Y. Huang, *Nat. Commun.*, 2015, **6**, 6929.
37 J. Wang, J. Polleux, J. Lim and B. Dunn, *J. Phys. Chem. C*, 2007, **111**, 14925–14931.
38 Z. Hu, Z. Q. Zhu, F. Y. Cheng, K. Zhang, J. B. Wang, C. C. Chen and J. Chen, *Energy Environ. Sci.*, 2015, **8**, 1309–1316.